

Long-term excitation energy transfer predicted by a modified convolutional neural networks in the FMO complexes

Yi-Meng Huang,¹ Zi-Ran Zhao,^{1,*} and Shun-Cai Zhao^{1,†}

¹*Center for Quantum Materials and Computational Condensed Matter Physics,
Faculty of Science, Kunming University of Science and Technology, Kunming, 650500, PR China*

(Dated: 00:21, Wednesday 26th March, 2025)

In machine learning (ML), the risk of recursive strategies overfitting historical data has driven the development of convolutional neural networks (CNNs) in simulating quantum dissipative dynamics. In this work, we propose an efficient CNNs scheme incorporating novel redundant time-functions to predict 100 picosecond (ps) excitation energy transfer (EET) in Fenna-Matthews-Olson (FMO) complexes, in which the original time t is normalized by mapping it to the $[0, 1]$ range, allowing different functions focus on distinct time intervals, thereby effectively capturing the multi-timescale characteristics of EET dynamics. This method simplifies optimization and enhances learning efficiency, and demonstrate the superior accuracy, robustness, and efficiency of our approach in predicting quantum dissipative dynamics.

CONTENTS

I. Introduction	1
II. Theoretical Model	2
A. Quantum dynamics of the FMO complex	2
B. Novle redundant time-functions	3
C. Data architecture of CNN	4
III. Results and discussions	4
A. Training model validation	4
B. Long-term prediction of EET	5
IV. Conclusion and outlook	7
Code availability	7
Author contributions	7
V. Acknowledgment	7
Data Availability Statement	7
Conflict of Interest	7
References	7

I. INTRODUCTION

The nearly 100% photosynthetic conversion efficiency observed in photosynthetic organisms, such as the Fenna-Matthews-Olson (FMO) complex, has sparked considerable research interest[1–3]. This remarkable efficiency is a key prerequisite for the development of artificial photosynthetic devices[4–6]. Understanding and simulating the excitation energy transfer (EET) dynamics in the FMO complex is essential for unraveling the physics behind its remarkable efficiency. EET dynamics are typically described within the framework of open system theory, which is governed by the Hamiltonian evolution of the total system and characterized by the reduced density operator[2, 3, 7]. Several numerically exact methods have been developed to simulate the reduced dynamics, including the hierarchy of equations of motion (HEOM) technique[8], path-integral Monte Carlo[9], multi-configurational time-dependent Hartree (MCTDH)[10], the stochastic Liouville-von Neumann equation[11], time-evolving density matrix using orthogonal polynomials algorithm (TEDOPA)[12], etc. However, modeling the influence of the environment on quantum systems presents significant challenges due to the vast number of environmental degrees of freedom[13], limiting their practicality for investigating long-term quantum dynamical phenomena.

* Co-first author.

† Corresponding author: zsczhao@126.com.

In recent years, machine learning (ML) has emerged as a powerful tool for simulating quantum dissipative dynamics[14–20]. Among these approaches, recursive ML strategies predict future dynamics based on historical data[21–24], resembling traditional quantum dynamics where the system’s evolution explicitly depends on its current state and implicitly on prior states. However, these recursive methods often suffer from overfitting to past data, as well as from issues like gradient disappearance or explosion, which may violate fundamental physical principles such as trace conservation of the density matrix. To address these challenges, convolutional neural networks (CNNs)[17, 23] have been proposed as a more effective approach for predicting quantum dynamical evolution, aiming to overcome the limitations of recursive methods and better preserve the system’s physical constraints.

In this work, we adopt a refined spatiotemporal mapping approach with the Quantum Toolbox in Python (QuTiP)[25] in combination with CNNs. After collecting EET dynamics data from the FMO complex through numerical simulations, we endow the data with specific physical connotations by integrating the evolution of time with the physical laws governing EET dynamics, where time redundant-functions are explicitly reflected. Consequently, time points that were previously unrelated to physical systems are now incorporated as features in the CNNs.

Consequently, time points that were previously unrelated to physical systems are now incorporated as features in the CNNs. Additionally, the intrinsic correlations between chlorophyll sites in the FMO complex are incorporated into the label construction, providing the neural network with a solid physical foundation. This refined spatiotemporal mapping allows the model to make accurate predictions in both temporal (from 7 to 100 ps) and spatial extrapolations (using environmental parameters outside the training set). As a result, the model’s stability and performance are significantly enhanced, effectively preventing issues such as gradient disappearance and explosion that typically arise in long-term numerical simulations.

II. THEORETICAL MODEL

A. Quantum dynamics of the FMO complex

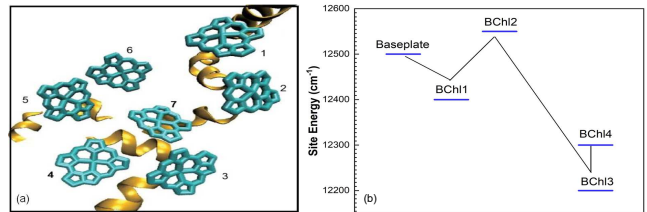


FIG. 1. (a) Seven bacteriochlorophyll (BChl) molecules in the FMO pigment-protein complex. (b) The energy transfer pathways in the FMO complex: baseplate \rightarrow BChls 1 \rightarrow 2 \rightarrow 3 \rightarrow 4 with the initial excitation BChl 1.

The energy flow within the FMO complex has been shown to primarily occur through two main excitation energy transfer (EET) pathways[26]. These pathways link bacteriochlorophylls (BChls) that are spatially close and excitonically coupled, as demonstrated by Brixner et al. leveraging a two-dimensional electronic spectroscopy[27]. In the subsequent analysis, we will examine the quantum dynamics of EET based on the energy flow pathways depicted in Fig.1(b). The Hamiltonian governing this process comprises three components: the electronic state Hamiltonian \hat{H}_e , the environmental phonon Hamiltonian \hat{H}_{ph} , and the electron-phonon interaction Hamiltonian \hat{H}_{el-ph} [28], as follows:

$$\hat{H}_t = \hat{H}_e + \hat{H}_{ph} + \hat{H}_{el-ph}, \quad (1)$$

$$\hat{H}_e = \sum_{j=1}^7 \epsilon_j |j\rangle \langle j| + \sum_{h=1, h \neq j}^7 J_{jh} |j\rangle \langle h|, \quad (2)$$

$$\hat{H}_{ph} = \sum_{\xi} \hbar \omega_{\xi} \hat{b}_{\xi}^{\dagger} \hat{b}_{\xi}, \quad (3)$$

$$\hat{H}_{el-ph} = \sum_{j=1}^7 (\lambda_j + \hat{u}_j) |j\rangle \langle j|, \quad (4)$$

$$\hat{u}_j = - \sum_{\xi} c_{j\xi} \hat{q}_{\xi}. \quad (5)$$

Each pigment is modeled as a two-level system, where $|j\rangle$ denotes the excited state of the j -th pigment molecule. Here, ϵ_j represents the site energy of the j -th pigment molecule in Eq.(2), and J_{jk} describes the electronic

coupling strength between the j -th and j -th pigment molecules.

In the expression for \hat{H}_{ph} given by Eq.(3), ω_ξ is the frequency of the ξ -th phonon mode, while \hat{b}_ξ^\dagger and \hat{b}_ξ are the creation and annihilation operators of the ξ phonon mode, respectively. In Eq.(4), λ_j represents the reorganization energy at site j , modeled using the continuous Drude-Lorentz spectral density as described in Eq.(6).

$$J_j(\omega) = 2\lambda_j \frac{\omega\gamma_j}{\omega^2 + \gamma_j^2} \quad (6)$$

Considering the influence of discrete molecular modes on population dynamics[29], $c_{j\xi}$ in Eq.(5) represents the coupling constant between the j -th pigment molecule and the ξ -th phonon mode, while \hat{q}_ξ denotes the dimensionless coordinate of the ξ -th phonon mode. The reference quantum dynamics trajectories for the reduced density matrix of the system are propagated using the local thermalizing Lindblad master equation[30]. The Adolphs and Renger Hamiltonian, describing seven sites per subunit[31], is employed as follows:

$$\begin{bmatrix} 200 & -87.7 & 5.5 & -5.9 & 6.7 & -13.7 & -9.9 \\ -87.7 & 320 & 30.8 & 8.2 & 0.7 & 11.8 & 4.3 \\ 5.5 & 30.8 & 0 & -53.5 & -2.2 & -9.6 & 6.0 \\ -5.9 & 8.2 & -53.5 & 110 & -70.7 & -17.0 & -63.3 \\ 6.7 & 0.7 & -2.2 & -70.7 & 270 & 81.1 & -1.3 \\ -13.7 & 11.8 & -9.6 & -17.0 & 81.1 & 420 & 39.7 \\ -9.9 & 4.3 & 6.0 & -63.3 & -1.3 & 39.7 & 230 \end{bmatrix}$$

The energies are given in cm^{-1} , with each site interacting independently with its surrounding environment, which is characterized by the Drude-Lorentz spectral density as described in Eq. (6).

B. Novel redundant time-functions

Accurately capturing time-dependent dynamics, such as the evolution of density matrices in quantum transport systems, is crucial for understanding molecular excited states. However, directly inputting raw time variables into neural networks can introduce several challenges: the presence of vast time scales, localized sensitivity in temporal resolution (which may lead to overfitting in certain intervals while underfitting others), and difficulties in handling infinite-time limits, such as steady states or relaxation endpoints.

To address these challenges, the concept of redundant time-functions has been incorporated into neural networks [17] to encode temporal information, thereby enhancing the model's robustness and expressiveness in describing time-dependent processes. Specifically, each logistic function is spaced by t ps apart and covers a local time window t . Collectively, the 100 logistic functions span from negative time to approximately $100t$ ps, enhancing the time resolution. This distributed temporal encoding, achieved through overlapping logistic functions, ensures that each time point is covered by multiple functions, akin to a sliding time window, thereby eliminating reliance on single-point inputs and improving multi-scale feature extraction. Inspired by this approach [17], we propose a refined redundant time-function, defined as:

$$f_k(t_n) = \frac{\eta_k(t_n) + g_k(t_n)}{14}, \quad (7)$$

$$\eta_k(t_n) = \tanh\left(\frac{t_n}{4} + \frac{k}{35}\right), \quad (8)$$

$$g_k(t_n) = \frac{13}{1 + 15 \exp[-0.02(40t_n + 4k - 1)]}. \quad (9)$$

The logistic function $f_k(t_n)$ exhibits smooth S-shaped characteristics, allowing the original time t to be mapped onto the $[0, 1]$ range, thereby normalizing the time input. To improve prediction accuracy, we incorporated the \tanh function (Eq.(8)) in addition to modifying the logistic function (Eq.(9)).

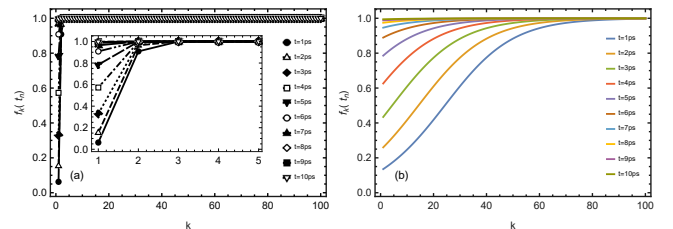


FIG. 2. Evolutions of redundant time-functions $f_k(t_n)$ with respect to parameter k at different moments, $k \in \{0, 1, 2, \dots, 99\}$. (a) Redundant time-functions in Ref.[17] with an inset displaying for $k \in [0, 5]$. (b) Novel redundant time-functions.

As shown in Ref.[17], the redundant time-functions achieve normalization only when $k \geq 3$ (as illustrated in Fig. (2)(a)). In contrast, the functions proposed in

this work (Fig. 2(b)) exhibit significantly enhanced robustness and superior performance in long-term predictions. These functions achieve normalization across distinct time intervals, including early-stage rapid evolution, mid-stage transitions, and long-term steady states, thereby effectively capturing the multi-timescale characteristics of quantum dynamics. Moreover, even in the presence of parameter fluctuations or noise, the redundancy introduced through numerous overlapping logistic functions ensures that alternative functions remain effective in providing temporal information. This design enhances fault tolerance, guaranteeing the complete encoding of the dynamical process from transient behavior to steady state, thereby preventing information loss and ensuring full-time coverage. Consequently, these refined redundant time-functions serve as critical input features for convolutional neural networks (CNNs), enabling them to efficiently learn complex dynamical laws and accurately predict the long-term evolution of quantum system configurations.

C. Data architecture of CNN

(Energy level)/10	γ_n	λ_b	T_c	$\{f_k(t_n)\}$	$\{\rho_{ii}(t_n)\}$	$\sum_{i=1}^6 Abs(\rho_{ii} - \rho_{i+1,i+1})$	$\sum_{i=1}^7 \rho_{ii}(t_j)$
0.1	γ_1	λ_1	T_1	$f_k(t_n)$	$\rho_{11}(t_n)$	$Abs(\rho_{11}(t_n) - \rho_{22}(t_n))...$	$\rho_{11}(t_n) + \rho_{22}(t_n)...$
\vdots	\vdots	\vdots	\vdots	\vdots	\vdots	\vdots	\vdots
0.1	γ_1	λ_1	T_1	$f_k(t_m)$	$\rho_{11}(t_m)$	$Abs(\rho_{11}(t_m) - \rho_{22}(t_m))...$	$\rho_{11}(t_m) + \rho_{22}(t_m)...$
0.1	γ_2	λ_1	T_1	$f_k(t_n)$	$\rho_{11}(t_n)$	$Abs(\rho_{11}(t_n) - \rho_{22}(t_n))...$	$\rho_{11}(t_n) + \rho_{22}(t_n)...$
\vdots	\vdots	\vdots	\vdots	\vdots	\vdots	\vdots	\vdots
0.1	γ_2	λ_1	T_1	$f_k(t_m)$	$\rho_{11}(t_m)$	$Abs(\rho_{11}(t_m) - \rho_{22}(t_m))...$	$\rho_{11}(t_m) + \rho_{22}(t_m)...$
\vdots	\vdots	\vdots	\vdots	\vdots	\vdots	\vdots	\vdots
0.1	γ_m	λ_1	T_1	$f_k(t_n)$	$\rho_{11}(t_n)$	$Abs(\rho_{11}(t_n) - \rho_{22}(t_n))...$	$\rho_{11}(t_n) + \rho_{22}(t_n)...$
0.1	γ_1	λ_2	T_1	$f_k(t_n)$	$\rho_{11}(t_n)$	$Abs(\rho_{11}(t_n) - \rho_{22}(t_n))...$	$\rho_{11}(t_n) + \rho_{22}(t_n)...$
\vdots	\vdots	\vdots	\vdots	\vdots	\vdots	\vdots	\vdots
0.1	γ_1	λ_j	T_1	$f_k(t_n)$	$\rho_{11}(t_n)$	$Abs(\rho_{11}(t_n) - \rho_{22}(t_n))...$	$\rho_{11}(t_n) + \rho_{22}(t_n)...$
0.1	γ_1	λ_1	T_2	$f_k(t_n)$	$\rho_{11}(t_n)$	$Abs(\rho_{11}(t_n) - \rho_{22}(t_n))...$	$\rho_{11}(t_n) + \rho_{22}(t_n)...$
\vdots	\vdots	\vdots	\vdots	\vdots	\vdots	\vdots	\vdots
0.1	γ_1	λ_1	T_j	$f_k(t_n)$	$\rho_{11}(t_n)$	$Abs(\rho_{11}(t_n) - \rho_{22}(t_n))...$	$\rho_{11}(t_n) + \rho_{22}(t_n)...$

TABLE I. Parameters used in the training structure for convolutional neural network (CNN) architecture: labels for chlorophyll sites were divided by 10, i.e., the input elements corresponding to the columns in the reduced density matrix are $\{0.1, 0.2, 0.3, \dots, 0.7\}$. Time-functions based on the logistic were defined as $f_k(t_n) = \frac{\eta_k(t_n) + g_k(t_n)}{14}$, $\eta_k(t_n) = \tanh(\frac{t_n}{4} + \frac{k}{35})$, $g_k(t_n) = \frac{13}{1+15 \exp[-0.02(40t_n+4k-1)]}$, $t_n = \{t_0, t_1, \dots, t_m\}$, $k \in \{0, 1, 2, \dots, 99\}$, $\gamma_a = \{\gamma_0, \gamma_1, \dots, \gamma_j\}$, $\lambda_b = \{\lambda_0, \lambda_1, \dots, \lambda_j\}$, $T_c = \{T_0, T_1, \dots, T_j\}$.

In this study, key physical parameters governing excitation

energy transfer (EET) were selected as features for the convolutional neural network (CNN). The reorganization energy (λ) characterizes the coupling strength between molecules and their environment, directly influencing energy transfer efficiency. The characteristic frequency (γ) describes the bath relaxation rate, reflecting the environment's response speed to excited-state evolution. Temperature (T) impacts thermal fluctuations and decoherence processes, thereby altering the quantum energy transfer efficiency. Additionally, the novel redundant time-functions were incorporated to normalize the temporal domain, facilitating the network's capacity to capture both short-term quantum beats and long-term asymptotic behavior. As presented in Tab. I, all relevant parameters are explicitly outlined in the Features column.

The learning objectives of the CNN, corresponding to the predicted outputs, serve as labels to represent the dynamical evolution of the FMO system. In contrast to Ref. [17], where only the diagonal elements $\rho_{jj}(t)$ were employed to represent exciton populations at each BChl site and track EET, this work expands the learning targets by introducing two additional labels: $\sum_{i=1}^6 Abs(\rho_{ii} - \rho_{i+1,i+1})$ and $\sum_{i=1}^7 \rho_{ii}(t_j)$. These complementary labels enhance the model's predictive accuracy, providing a more comprehensive description of EET dynamics. The aforementioned label data are clearly indicated in the labels column of Tab. I.

To prepare the dataset, several preprocessing steps were applied to ensure effective model training. The labels associated with the seven sites were scaled down by a factor of 10, resulting in normalized values ranging from 0.1 to 0.7. Additionally, λ was divided by 100, while γ and T were each divided by 1000 to standardize their magnitudes. Temporal variables were normalized leveraging 100 redundant time-functions $f_k(t_n)$, constructed from logistic functions with k ranging from 0 to 99. This preprocessing procedure effectively scales and normalizes the input data, ensuring that the CNN can accurately learn the underlying physical processes governing EET.

III. RESULTS AND DISCUSSIONS

A. Training model validation

To ensure the reliability of the CNN model, we validated it using a dataset spanning 7 picoseconds (ps), comprising 301 evenly distributed time points between 0 and 7 ps. The EET dynamic evolution trajectories for each site of the FMO complex were generated using the QuTiP method. These tra-

jectories, covering the 0 to 7 ps range (denoted as $m = 7$), were simulated under varying environmental parameters: reorganization energy (λ) ranging from 14 to 28 cm^{-1} , characteristic frequency (γ) from 150 to 164 cm^{-1} , and temperature

(T) from 270 to 284 K. Each environmental parameter was assigned 15 distinct values within its respective range. Based on this setup, the number of rows in Table I is determined by Eq. (10), the number of feature columns is calculated using Eq. (11), and the j -th label column is derived from Eq. (12).

$$N_{\text{rows}} = n_{\text{Energysites}} \times n_{\text{Timepoints}} \times n_{\gamma} \times n_{\lambda} \times n_T, \quad (10)$$

$$N_{\text{Features}} = n_{\text{Energysites}} + n_{\gamma} + n_{\lambda} + n_T + n_{f_k(t_m)}, \quad (11)$$

$$\text{Labels}_j = \text{Energysite}_j + \sum_{i=1}^6 [|\rho_{jj} - \rho_{i+1,i+1}| + (\rho_{jj} + \rho_{i+1,i+1})] \quad (12)$$

In Eq.(10)~(11), n represents the number of corresponding parameter, and the subscript j denotes the j -th site in Eq.(12). Following this procedure, a feature matrix with dimensions 7, 111, 125 \times 104 is constructed, accompanied by a label matrix of dimensions 7, 111, 125 \times 13. Transforming the dataset into this matrix format enables the CNN to efficiently process the data while maintaining high predictive accuracy, making it a suitable choice for training and prediction.

In the resulting matrix, the first column corresponds to the population value of the current energy level at a given time. Columns 2~7 contain the absolute values of the population differences between the current energy level and the others at that same time, while columns 8~13 represent the sums of the populations of the current energy level and the others at that moment. Subsequently, the convolutional output matrix is compared with the label matrix to compute the loss, for which the mean squared error (MSE) is adopted in this study. Through iterative backpropagation and continuous optimization, the final CNN model is obtained ([Codes-for-CNN](#)).

In Fig. 3, the CNN model incorporating the refined redundant time-functions was validated for predicting the evolution of the seven-site configuration over a 7 ps timescale. Under the given environmental parameters ($\lambda = 15 \text{ cm}^{-1}$, $\gamma = 175 \text{ cm}^{-1}$, and $T = 155 \text{ K}$), the green solid lines (theoretical values) and the black dashed lines (CNN-predicted values) exhibit near-complete overlap, indicating a strong agreement between the theoretical calculations and the model's predictions.

Traditional quantum dynamics simulations typically employ recursive methods, where each step's prediction depends on the outcome of the previous step. This recursive nature can lead to error accumulation over time, compromising long-term accuracy. In contrast, the CNN-based approach presented here is non-recursive, circumventing the need for step-wise computation of the evolution trajectory. Instead, the

CNN directly predicts the excitation energy transfer (EET) dynamics across the entire temporal domain. This architecture not only prevents error propagation but also substantially reduces computational costs, enhancing both efficiency and prediction accuracy.

B. Long-term prediction of EET

The CNN model incorporating redundant time-functions, as shown in Fig. 3, effectively captures the detailed evolution of the seven-site configuration over a 7-picosecond timescale. Building on the refined redundant time-functions and the distinct labels introduced in this work, we further explored the system's dynamical behavior over longer timescales. To achieve this, data from the 0~7 ps period were collected using the QuTiP tool, serving as the training set for predicting the dynamical evolution of the FMO complex over the 7~100 ps timeframe. The environmental parameters for training were set as follows: λ : 28~30 cm^{-1} , γ : 164~170 cm^{-1} , T : 284~290 K.

In Fig. 4, the population predictions for each chlorophyll site are extended to 100 ps, with both the predicted results and theoretical calculations plotted on the same graph for direct comparison. To better illustrate the population dynamics over an extended timescale, logarithmic scales are applied to the insets of each panel. The green solid lines, representing theoretical values, and the black dotted lines, denoting predicted results, exhibit remarkable agreement over the 100-ps period. Notably, around the 10-ps mark, the population dynamics of the FMO system show a tendency toward stabilization, consistent with the findings reported in Ref. [17]. The incorporation of modified redundant time-functions in this work significantly extends the prediction timeframe, offering a more comprehensive perspective on the long-term popula-

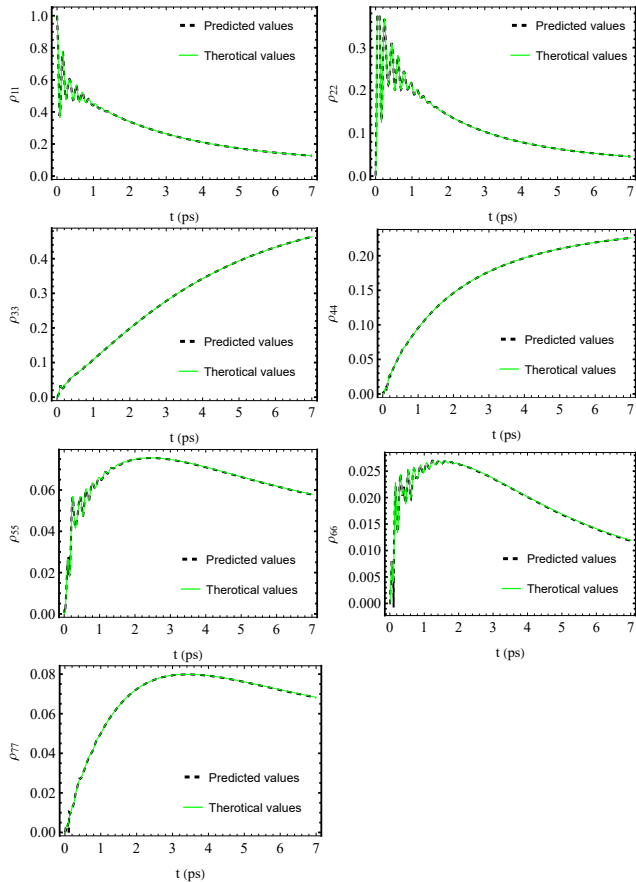


FIG. 3. Population dynamics of the seven chlorophyll sites with green solid lines being theoretical values and black dashed lines being predicted values in the FMO complex within 7 ps. Other parameters are $\lambda=15 \text{ cm}^{-1}$, $\gamma=275 \text{ cm}^{-1}$, $T=155 \text{ K}$.

tion evolution.

Compared with the 2.5-picosecond prediction reported in Ref [17], the superior performance of this proposed CNN in accurately predicting the time evolution of EET can be attributed to several key factors, which are discussed below.

First, the CNN's exceptional feature extraction capability enables it to capture short-term dynamic features in temporal evolution by leveraging convolutional kernels to process input data, effectively identifying intrinsic correlations in energy distributions across different time points. Second, the CNN's translation invariance allows it to recognize recurring dynamic patterns regardless of their temporal position, enhancing its robustness in predicting long-term evolution. Third, the network's multi-layer architecture facilitates hierarchical feature extraction, where pooling layers reduce data dimensionality while preserving essential features, thereby improving computational efficiency and mitigating overfitting.

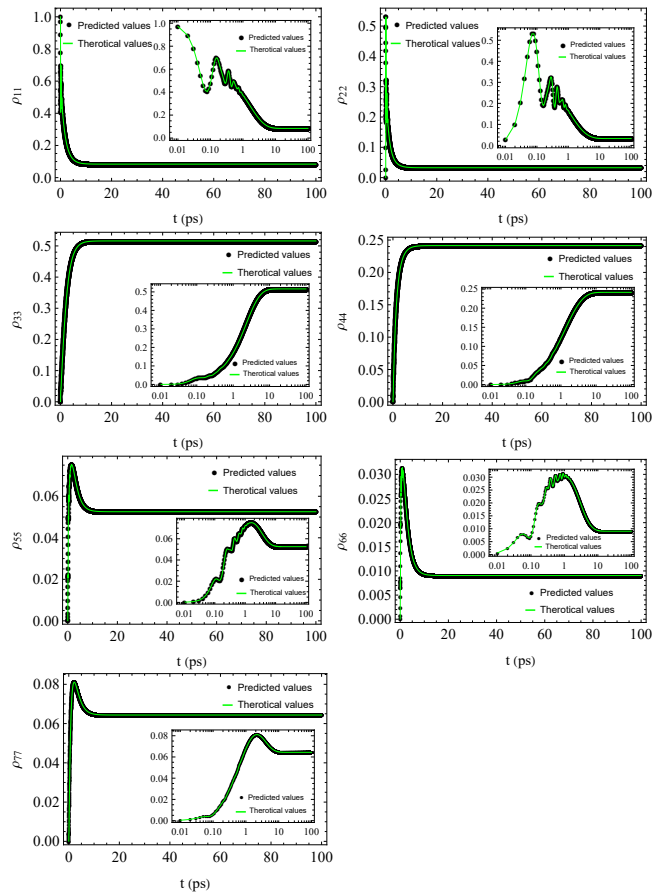


FIG. 4. Population dynamics of the seven chlorophyll sites with green solid lines being theoretical values and black dotted lines being predicted values in the FMO complex within 100 ps. The inset plots are in logarithmic scale. Other parameters are $\lambda=30 \text{ cm}^{-1}$, $\gamma=286 \text{ cm}^{-1}$, $T=166 \text{ K}$.

Moreover, unlike traditional time-evolution simulations that rely on recursive methods, where predictions at each step depend on previous outputs, leading to cumulative errors, while the CNN employs a non-recursive prediction mechanism. By extracting features from the entire time window in a single operation, the model directly outputs long-term evolution results, effectively circumventing error propagation. Crucially, the introduction of redundant time-functions (Eq.7) further enhances predictive accuracy, extending the model's capability to capture long-term EET dynamics beyond the performance reported in Ref.[17]. This methodological advancement extends the model's predictive power to longer timescales, offering deeper insights into the quantum dynamics of the system.

IV. CONCLUSION AND OUTLOOK

In summary, this work introduces a novel redundant time-function as a CNN input feature and uses distinct labels to predict EET dynamics across seven sites in the FMO complex, where the temporal evolution was explicitly partitioned into distinct regimes (rapid, transitional, and steady-state). These functions, combined with physically informed labels encoding population differences and sums, enable CNNs to achieve quantitative agreement with theoretical benchmarks in simulating 100 ps EET across all seven chlorophyll sites of the FMO complex. Crucially, the method eliminates error propagation inherent to recursive strategies, demonstrating robustness. This approach not only validates CNNs for long-term quantum dynamics prediction but also provides a generalizable architecture for modeling dissipative processes. By bridging machine learning with quantum physics, the framework offers a scalable pathway to optimize artificial light-harvesting systems and accurately forecasts long-term quantum system dynamics under various external conditions.

CODE AVAILABILITY

The code is available at: [Codes-for-CNN](#) and [Codes-for-all-Figs](#).

AUTHOR CONTRIBUTIONS

S. C. Zhao conceived the idea. Y. M. Huang performed the numerical computations and wrote the draft, and S. C.

Zhao did the analysis and revised the paper. Z. R. Zhao participated in part of the discussion.

V. ACKNOWLEDGMENT

We thank the financial supports from the National Natural Science Foundation of China (Grant Nos. 62065009 and 61565008), and the General Program of Yunnan Applied Basic Research Project, China (Grant No. 2016FB009).

DATA AVAILABILITY STATEMENT

This manuscript has associated data in a data repository. [Authors' comment: All data included in this manuscript are available upon reasonable request by contacting with the corresponding author.]

CONFLICT OF INTEREST

The authors declare that they have no conflict of interest. This article does not contain any studies with human participants or animals performed by any of the authors. Informed consent was obtained from all individual participants included in the study.

-
- [1] F. H. Alharbi and S. Kais, *Renew. and Sustain. Ener. Rev.* **43**, 1073 (2014), [arXiv:1105.4189 \[quant-ph\]](#).
- [2] L. F. Li, S. C. Zhao, and L. X. Xu, *Chin. Phys.s B* **30**, 044215 (2021).
- [3] L. F. Li, S. C. Zhao, and L. X. Xu, *Europ Phys J Plus* **136**, 1 (2021).
- [4] S. Maity, B. M. Bold, J. D. Prajapati, M. Sokolov, T. Kubar, M. Elstner, and U. Kleinekathfer, *J Phys. Chem. Lett.* **11**, 8660 (2020).
- [5] J. Schulze, M. F. Shibl, M. J. Al-Marri, and O. Kuhn, *J Chem. Phys.* **144** **18**, 185101 (2016), [arXiv:1602.03973 \[quant-ph\]](#).
- [6] I. G. Karafyllidis, *J. Bio. Phys.* **43**, 239 (2017).
- [7] P. Huo and T. F. Miller, *Phys Chem. Chem. Phys.* **17** **46**, 30914 (2015).
- [8] Y. Tanimura, *J. Chem. Phys.* **153** **2**, 020901 (2020).
- [9] D. Kast and J. Ankerhold, *Phys. Rev. Lett.* **110** **1**, 010402 (2012).
- [10] H.-D. Meyer, U. Manthe, and L. S. Cederbaum, *Chem. Phys. Lett.* **165**, 73 (1990).
- [11] J. T. Stockburger and H. Grabert, *Phys. Rev. Lett.* **88** **17**, 170407 (2002).
- [12] J. Prior, A. W. Chin, S. F. Huelga, and M. B. Plenio, *Phys. Rev. Lett.* **105** **5**, 050404 (2010).
- [13] A. J. Leggett, S. Chakravarty, A. T. Dorsey, M. P. A. Fisher, A. Garg, and W. Zwerger, *Rev. Mod. Phys.* **59**, 1 (1987).

- [14] S. Hochreiter and J. Schmidhuber, *Neural Computation* **9**, 1735 (1997).
- [15] K. Lin, J. Peng, F. L. Gu, and Z. Lan, *J Phys. Chem. Lett.* **12**, 10225 (2021), arXiv:2108.01310 [quant-ph].
- [16] D. Lemm, G. F. von Rudorff, and O. A. von Lilienfeld, *Nat. Comm.* **12**, 4468 (2021), arXiv:2102.02806 [physics.chem-ph].
- [17] A. Ullah and P. O. Dral, *Nat. Comm.* **13** (2022).
- [18] K. Naicker, I. Sinayskiy, and F. Petruccione, *Phys. Rev. Research* **4**, 033175 (2021), arXiv:2112.11889 [quant-ph].
- [19] Y. Han, I. Ali, Z. Wang, J. Cai, S. c. Wu, J. Tang, L. Zhang, J. Ren, R. Xiao, Q. Lu, L. Hang, H. Luo, and J. Li, *Phys. Rep.* **934**, 1 (2021).
- [20] K. Lin, J. Peng, C. Xu, F. L. Gu, and Z. Lan, *J. Chem. Theor. and Comput.* **18**, 5837 (2022), arXiv:2205.03600 [quant-ph].
- [21] A. Ullah and P. O. Dral, *New J. Phys.* **23** (2021).
- [22] L. E. H. Rodríguez, A. Ullah, K. J. R. Espinosa, P. O. Dral, and A. A. Kananenka, *Machine Learning: Sci. and Tech.* **3** (2022).
- [23] L. E. H. Rodríguez and A. A. Kananenka, *J. Phys. Chem. Lett.* , 2476 (2020).
- [24] L. E. H. Rodríguez and A. A. Kananenka, *J Chem. Phys.* **161** **17** (2024).
- [25] J. Johansson, P. D. Nation, and F. Nori, *Comput. Phys. Commun.* **183**, 1760 (2011), arXiv:1110.0573 [quant-ph].
- [26] R. E. Fenna and B. W. Matthews, *Nature* **258**, 573 (1975).
- [27] T. Brixner, J. Stenger, H. M. Vaswani, M. Cho, R. E. Blankenship, and G. R. Fleming, *Nature* **434**, 625–628 (2005).
- [28] A. Ishizaki and G. R. Fleming, *PNAS* **106**, 17255 (2009).
- [29] P. Nalbach and M. Thorwart, *J. Phys. B* **45**, 154009 (2012).
- [30] M. Mohseni, P. Rebentrost, S. Lloyd, and A. Aspuru-Guzik, *J. Chem. Phys.* **129**, 174106 (2008).
- [31] J. Adolphs and T. Renger, *Biophysical Journal* **91**, 2778 (2006).